NJC

PAPER

View Article Online
View Journal | View Issue

Cite this: *New J. Chem.*, 2015, 39, 6593

Shell decoration of hydrothermally obtained colloidal carbon spheres with base metal nanoparticles†

Jacco Hoekstra,[a] Andrew M. Beale,[bcd] Fouad Soulimani,[b] Marjan Versluijs-Helder,[b] John W. Geus[a] and Leonardus W. Jenneskens*[a]

Received (in Montpellier, France) 31st March 2015,
Accepted 30th June 2015

DOI: 10.1039/c5nj00804b

www.rsc.org/njc

The preparation of base metal nanoparticles supported on the shell of colloidal carbon spheres (CCS) is reported. Hydrothermal treatment of a sucrose solution gave conglomerates of *ca.* 30 μm of CCS (diameter 2–8 μm), which consist of a hydrophobic core with a hydrophilic shell due to the presence of oxygen containing functional groups. The CCS were loaded by wet impregnation with various metal salts (copper, nickel, cobalt, iron). Subsequent pyrolysis under inert conditions at T = 800 °C led to the carbothermal reduction of the impregnated metal salts by the support material. The base metal nanoparticles (size *ca.* 35–70 nm) are supported on the circumference of the CCS in line with its core–shell structure. Moreover, in the case of nickel, cobalt and iron nanoparticles, all capable of forming metastable metal carbides, the carbonised shells are converted into nanostructures of graphitic carbon, *viz.*, catalytic graphitisation occurs. The spheres were characterised by scanning- and transmission electron microscopy, X-ray diffraction, Raman spectroscopy, elemental analysis, infrared spectroscopy and thermogravimetric analysis.

1. Introduction

Hydrothermal carbonisation (HTC) is a thermochemical process for the benign conversion of carbon-based precursors, such as biomass, into solid coal-like products. During an exothermic process the hydrogen and oxygen content of these precursors is reduced *via* consecutive dehydration and decarboxylation reactions. To this end, the precursor is either dissolved or dispersed in water in an autoclave and heated at T = 160–250 °C at autogenous pressure.[1]

HTC of monomeric and dimeric carbohydrates, such as glucose and sucrose, yields monodisperse nanometer- or micrometer-sized colloidal carbon spheres (CCS) of 150–1500 nm in diameter.[2,3] Their diameter can be controlled by fine-tuning the experimental conditions (initial concentration of the aqueous carbohydrate solution, temperature and reaction time). CCS formation from carbohydrates occurs in consecutive steps. Firstly, intra- and intermolecular dehydration of the carbohydrate takes place to yield (primarily) furanic compounds (*e.g.* hydroxymethylfurfural). Secondly, these intermediate products undergo further dehydration and fragmentation reactions (*i.e.* ring opening and C–C bond breaking) followed by polymerization. When the solution reaches critical supersaturation, finally a nucleation process is induced, which leads to a rapid formation of CCS at T = 160–250 °C.[3–5] The CCS consist of a hydrophobic aromatic core with stable oxygen functionalities (*e.g.* ethers and quinones, with furan rings as structural units) with a hydrophilic shell due to the presence of reactive oxygen-containing functional groups (*e.g.* hydroxyl-, carbonyl-, and carboxyl-moieties).[6,7]

The synthesis of functional materials *via* HTC and their (potential) application in a variety of scientific areas is drawing considerable attention.[8–10] Hydrothermally produced carbonaceous materials have, for example, already been used in environmental

[a] *Organic Chemistry and Catalysis, Debye Institute for Nanomaterials Science, Utrecht University, Universiteitsweg 99, 3584 CA Utrecht, The Netherlands. E-mail: l.w.jenneskens@uu.nl*
[b] *Inorganic Chemistry and Catalysis, Debye Institute for Nanomaterials Science, Utrecht University, Universiteitsweg 99, 3584 CA Utrecht, The Netherlands*
[c] *UK Catalysis Hub, Research Complex at Harwell, Rutherford Appleton Laboratory, Harwell, Didcot, Oxfordshire, OX11 oFA, UK*
[d] *Department of Chemistry, University College London, 20 Gordon Street, London WC1H, oAJ, UK*

† Electronic supplementary information (ESI) available: Fig. S1; FT-IR spectrum of the CCS after work-up.[63] Fig. S2; Ellingham diagrams of the carbothermal reduction of the base metal oxides: copper (a), nickel (b), cobalt (c) and iron (d). Fig. S3; the original CCS (left) and the CCS after pyrolysis at T = 800 °C (right) in a biphasic system of water/hexane. Fig. S4; deconvolution results of the first-order (a) and second-order (b) Raman spectrum of the CCS after pyrolysis at T = 800 °C (* = N_2). Fig. S5; TGA (air) of CCS-supported base metal nanoparticles after pyrolysis at T = 800 °C. Fig. S6; Raman spectra of CCS loaded with copper (a), nickel (b) and cobalt (c) after pyrolysis at T = 800 °C (* = N_2). Table S1; elemental analysis and atomic ratios of sucrose and CCS samples. Table S2; deconvolution results of the Raman spectra of the CCS samples loaded with base metal nanoparticles after pyrolysis at T = 800 °C. See DOI: 10.1039/c5nj00804b

(CO_2 sequestration)[11,12] and electrical (fuel cells and batteries),[13] as well as opto-electronic[14] applications and catalyst supports for precious metals.[3,15,16]

To our knowledge only three reports have addressed the use of base metals in combination with HTC of carbohydrates. HTC of glucose in the presence of Fe_3O_4 nanoparticles yielded Fe_3O_4 nanoparticles embedded within the CCS.[17] Subsequent pyrolysis (T = 1300 °C) under N_2(g) led to the carbothermal reduction of the Fe_3O_4 nanoparticles to iron nanoparticles which catalytically converted the CCS to a porous graphitic material. In another investigation the addition of iron(III) nitrate during HTC of glucose gave Fe_xO_y nanoparticles embedded within the CCS.[18] Reduction using an external H_2(g) source of the Fe_xO_y nanoparticles to iron nanoparticles (T = 400 °C) resulted in an active Fischer–Tropsch catalyst. The addition of iron(III) nitrate and glucose during HTC and subsequent pyrolysis provided iron nanoparticles supported within the CCS.[19]

For applications, particularly in the liquid-phase (catalysis[20] and remediation[21]), it is beneficial to deposit the active metal nanoparticles only on the surface of a support material. Note that diffusion in the liquid-phase is relatively slow, with diffusion coefficients about a factor 10^4 lower than in the gas-phase.[20] Consequently, the surface of nanoparticles supported within the interior of a support material will have limited accessibility for reactants (catalysis) or contaminants (remediation), especially in the liquid-phase. Clearly, when the nanoparticles are deposited at the perimeter of the support material these diffusion limitations will be prevented.

The morphology of the CCS containing a shell of hydrophilic oxygen functionalities marks them interesting materials for further exploration. The functional groups enable a facile deposition of nanoparticles onto the surface of the CCS. This has already been demonstrated by the application of easily reducible precious metal nanoparticles (gold, silver, platinum, and palladium) onto the surface of the CCS. Note that in these cases reduction into the precious metal nanoparticles is achieved making use of the surface carbonyl groups,[3,15,16] resembling the known Tollens process.[22]

Reduction of base metal (copper, nickel, cobalt, iron) oxides, however, cannot be achieved. Copper, for instance can only be reduced from Cu^{2+} to Cu^{+} with aldehyde functional groups (Fehling's reagent[23]), further reduction to metallic copper does not occur. Alternatively, an external H_2(g) source can be used as the reducing agent. This is not preferable in the case of hydrophilic CCS. Firstly, it has been reported that water (vapour) strongly impairs the H_2(g) reduction to access metallic iron from Fe^{3+}/Fe^{2+}.[24] Secondly, H_2(g) reduction will lead to gasification of the CCS support material with hydrogenation catalysts such as nickel or cobalt,[25] resulting in excessive sintering. Thirdly, the wide explosion limits of hydrogen[26] are unattractive, particularly on an industrial scale. Recently we reported the carbothermal reduction of base metal oxides with carbon resulting from cellulose pyrolysis.[27] Here we investigate the reduction of base metal salts with the carbonaceous material from the CCS spheres, thereby circumventing the use of an external reducing agent.

Carbon nanomaterials, such as carbon nanofibers and few-layer graphene, are frequently employed as supports for nanoparticles. The surface of these materials is relatively inert. Treatment with severe oxidizing agents is required to introduce oxygen containing functionalities[28–33] which serve as adsorption sites of the nanoparticle precursors (metal salts). These oxygen containing functionalities are already beneficially available on the CCS surface.

Hence, our objective is to prepare base metal nanoparticles supported on the perimeter of the CCS making use of the reducing properties of the carbon support (carbothermal reduction). Therefore CCS obtained *via* HTC of an aqueous sucrose solution were loaded *via* wet impregnation with the metal salts of copper, nickel, cobalt or iron. Upon pyrolysis at T = 800 °C under a stagnant N_2(g) atmosphere the respective metal nanoparticles were obtained. The resulting shell-decorated CCS were characterized by scanning- and transmission electron microscopy (SEM, TEM) and X-ray diffraction (XRD). The influence of the reduced metal nanoparticles on the carbonaceous support material was investigated with high-resolution transmission electron microscopy (HR-TEM), XRD and Raman spectroscopy.

2. Experimental section

2.1. Chemicals

Sucrose ($C_{12}H_{22}O_{11}$, common table sugar) was purchased from the local supermarket and was used without further purification. The metal salts employed, $CuCl_2{\cdot}2H_2O$, $Ni(NO_3)_2{\cdot}6H_2O$, $Co(NO_3)_2{\cdot}6H_2O$ and $Fe(NO_3)_3{\cdot}9H_2O$ were purchased from Sigma-Aldrich (>98% purity) and were used as received.

2.2. Hydrothermal treatment of sucrose

Following the procedure reported in ref. 3 a 1 M sucrose (Spar®) solution (300 ml) in demineralised water was heated at T = 160 °C at autogenous pressure in a teflon-sealed autoclave for 4 h without stirring. The black CCS were isolated by centrifugation at 3000 rpm (Centaur 2 table centrifuge), redispersed in a 1 : 1 : 1 (v/v/v) mixture of acetone/ethanol/water (100 ml) followed by intense stirring and isolation by centrifugation. This procedure was repeated until a colourless liquid was obtained after washing (*ca.* 6 times). The resulting CCS were dried *in vacuo* ($p = 10^{-2}$ mbar) at room temperature to constant weight.

2.3. Preparation of CCS-supported metal nanoparticles

The hydrophilic CCS (2 g) were immersed in 10 ml of a 3 M aqueous solution of the respective metal salts. The CCS were left for 24 h within the solution under occasional stirring. The impregnated spheres were subsequently collected using a Büchner funnel with glass filter, after which the isolated spheres were dried *in vacuo* ($p = 10^{-2}$ mbar) at room temperature to constant weight. Next, the dried (loaded) spheres (1 g) were pyrolyzed in a stagnant N_2(g) atmosphere in a horizontally placed quartz glass tube of a Tube Furnace Reactor (TFR, Thermolyne 21100 furnace). Prior to pyrolysis the TFR was evacuated and refilled with N_2(g) thrice. Next, the oven was heated (heating rate 5 °C min^{-1}) to T = 800 °C, followed by isothermal pyrolysis for 1 h. After cooling to room temperature the product was brought into ambient atmosphere.

2.4. Characterization

Elemental analyses were performed by Dornis und Kolbe, Mikroanalytisches Laboratorium, Mülheim an der Ruhr, Germany.

Fourier transform infrared spectroscopy was performed with a Perkin-Elmer System 2000 spectrometer equipped with an ATR accessory (optical resolution 4 cm^{-1}).

Thermogravimetric analysis (TGA) was performed using a Perkin-Elmer Pyris 1 apparatus. A sample (5 mg) was heated under thermo-oxidative (air) conditions from T = 50 °C to T = 800 °C (heating rate 5 °C min^{-1}).

The external surface morphology of the CCS was examined in a Philips XL30 SFEG Scanning Electron Microscope (SEM). The spheres were attached to an aluminium stub by adhesive carbon tape. Secondary electron images provided the morphology of the surfaces of the spheres. The location of the heavier elements was apparent from back-scattered electron (SEM-BSE) images taken with a solid-state detector.

A FEG Tecnai-20 transmission electron microscope (TEM, FEI) equipped with a field-emission gun and a facility for scanning microscopy (STEM) gave information about the structure of the thermally treated spheres on a very small scale. The microscope was operated at 200 kV. The samples were prepared by grinding followed by ultrasonic dispersion in ethanol. A drop of the thus prepared suspension was applied onto a holey carbon film on top of a copper grid. A CCD camera at the bottom of the microscope was employed to obtain images at very high magnification exhibiting lattice images. For the recording of scanning electron micrographs a secondary electron detector and a HAADF (high-angle annular dark-field) detector were used. The HAADF detects the electrons scattered over a large angle; the images are dominated by heavier elements that are present.

Powder X-ray diffraction (XRD) patterns were obtained from 2θ = 10–80° on a Bruker-AXS X-ray diffractometer using CoKα_{12} radiation (λ = 0.17902 nm). The weight-mean average crystallite size (D) was calculated using the Scherrer equation:[34]

$$D = 0.94\lambda/(\Delta 2\theta \cos\theta), \quad (1)$$

in which 0.94 is a constant, λ the wavelength of the CoKα_{12} radiation, $\Delta 2\theta$ the angular width of the diffraction maximum at half of its maximum intensity (FWHM in radians) and θ the Bragg angle.

Raman spectra were recorded using a λ = 532 nm diode laser operating at 35 mW and a Holoprobe Kaiser Optical spectrometer equipped with a holographic notch filter and CCD camera. Data were collected on an isolated portion of the powdered sample for a period of 30 s over a range of 300–4300 cm^{-1}. The Raman data were analysed using the GRAMS/AI software suite, firstly to perform a multipoint manual baseline subtraction over the entire spectra, followed by curve fitting using the Levenberg–Marquardt algorithm. Peaks fitting was performed using predominantly Lorentzian components, though the broad band at *ca.* 1500 cm^{-1} was best approximated using a Gaussian function. A similar deconvolution protocol was applied and validated by Sadezky *et al.* in the deconvolution of the Raman spectra of numerous samples of soot, *viz.* carbonaceous materials.[35] To ensure an optimal fit of the data, the spectra were delineated and fitted in the so-called first-order region (800–1900 cm^{-1}) and second-order region (2100–3500 cm^{-1}) respectively. When fitting the data one band in the first-order spectra (1500 cm^{-1}) and one band in the second-order spectra (2700 cm^{-1}) were constrained to remain within *ca.* 50 cm^{-1} region of the spectra. The reduced χ^2 value was used to determine an optimal fit to the data and was always below 2%.

3. Results and discussion

3.1. Hydrothermal carbonization of sucrose

HTC of sucrose yielded a caramel-like brown, turbid, viscous and sweet smelling liquid in which a black precipitate was dispersed.[2,3] After work-up the CCS were obtained as a very fine black powder.

Conglomerates of the CCS are formed as can be inferred from SEM-BSE and STEM images (Fig. 1A and B). The diameter of the individual spheres is 2–8 μm. Note that the SEM image is obtained using the BSE detector. Using secondary electrons for imaging led to charging of the sample. Hence, the electrical conductivity of the pristine CCS spheres is low.

The presence of oxygen containing functionalities (C–O, C═O, COOH, OH) on the CCS is confirmed with Fourier transform infrared spectroscopy (Fig. S1, ESI†) and elemental analysis (Table S1, ESI†).[3] They ensure the hydrophilic character of the CCS perimeter and may serve as adsorption sites during impregnation with aqueous metal salt solutions (*vide infra*).

3.2. Carbothermal reduction

Thermal treatment of the metal salts under survey leads to the formation of the corresponding metal oxides between 200 and 300 °C.[36–39] Pyrolysis of the loaded CCS is expected to result in metal oxide nanoparticles supported on the perimeter of the CCS, since it is anticipated that during wet impregnation the metal salts will exclusively end up in the hydrophilic shell. At more elevated temperature, reduction of the metal oxide nanoparticles to metallic nanoparticles by the carbonaceous support may occur. Similar observations were made in related work in which metal salts were impregnated into microcrystalline cellulose spheres and subsequently pyrolyzed under an inert N_2(g) atmosphere.[27]

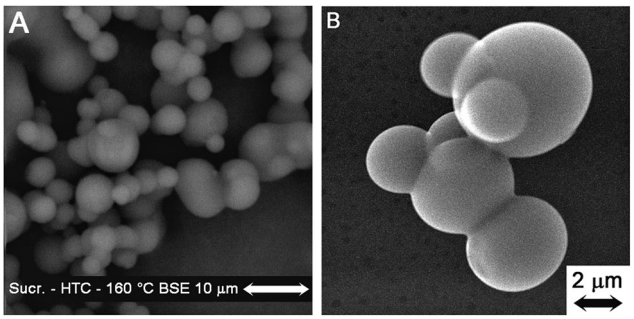

Fig. 1 SEM-BSE (A) and STEM image (B) of conglomerates of the CCS obtained from the HTC of sucrose at T = 160 °C.

From Ellingham diagrams (thermo-chemical database (HSC Chemistry 7.1, Outotec Oyj, Finland)), summarized in Fig. S2 (ESI†), the temperatures of carbothermal reduction of the relevant metal oxides were estimated. Thermodynamically, at T = 800 °C, all relevant metal oxides can be reduced with carbon, taking into account the Boudouard equilibrium.[40,41] Pyrolysis of CCS leads to a loss of the oxygen containing surface functional groups.[42] Most of the oxygen content appears to be removed after pyrolysis at T = 600 °C; a more or less stable oxygen content is found upon pyrolysis at T = 750 °C. Since the release of water (vapour) from the support surface is a prerequisite for the reduction of base metal oxide nanoparticles into metallic nanoparticles, a pyrolytic temperature of T = 800 °C was chosen.

3.3. Pyrolysis of the pristine CCS

To gain insight in the effect of the pyrolytic treatment on the CCS in the absence of metal ions, pyrolysis of the CCS under a stagnant $N_2(g)$ atmosphere at T = 800 °C was performed.

The CCS after thermal treatment at T = 800 °C are slightly more clustered than the pristine CCS (SEM image Fig. 2A). HR-TEM (Fig. 2B) shows that the CCS after pyrolysis consist of small graphitic sheets randomly folded together forming an amorphous carbonaceous material.

Elemental analysis (Table S1, ESI†) is in line with literature results,[42,43] although a higher oxygen content is found after pyrolysis at T = 800 °C (*ca.* 10 wt% *vs. ca.* 5 wt%). Notwithstanding, the hydrophilic shell is converted into a hydrophobic surface as is demonstrated in Fig. S3 (ESI†). Thus, the remaining oxygen content must represent the more stable bridged oxygen functionalities of the original core, while the oxygen functionalities of the periphery are lost.

Fig. 3 shows the XRD patterns of the pristine CCS and CCS after pyrolysis at T = 800 °C. A broad halo around 2θ = 26° is observed for both samples. The broadness and position of this d(002) reflection corresponds to the absence of stacking of graphitic layers confirming that an amorphous carbon is obtained.[44,45] The two dimensional lattice band at 2θ = 51° only becomes discernible after pyrolysis, which suggests that the small graphitic crystallites grow slightly in size, but that stacking of graphitic layers does not occur.

Raman spectroscopy, which is more sensitive to detect short-range disorder in carbonaceous materials, was also employed to characterize the CCS obtained after pyrolysis at T = 800 °C (Fig. 4). Curve fits of the first- and second-order regions are shown in Fig. S4 (ESI†); the deconvolution results are summarized in Table S2 (ESI†).

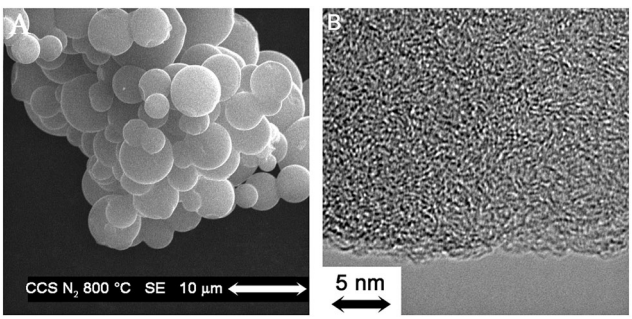

Fig. 2 SEM image of CCS after pyrolysis at T = 800 °C (A) and HR-TEM image of the amorphous carbon obtained (B).

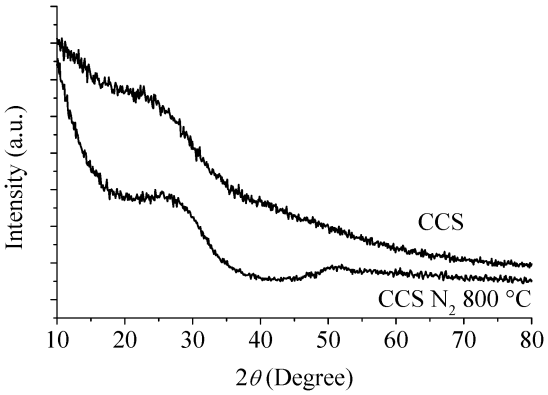

Fig. 3 XRD patterns of pristine CCS (top) and CCS after pyrolysis at T = 800 °C (bottom).

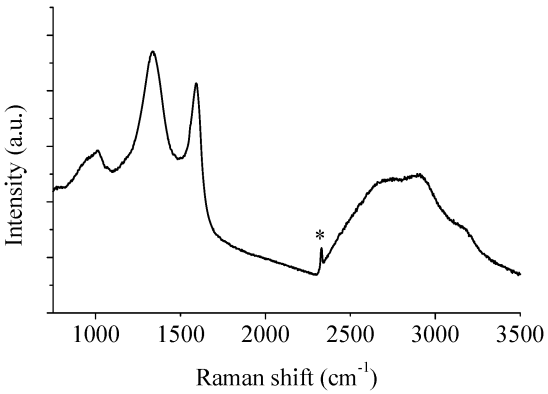

Fig. 4 Raman spectrum (first-order left, second-order right) of the CCS after pyrolysis at T = 800 °C. * = N_2.

Raman spectra of carbon materials consist of multiple bands.[35] The first-order spectrum of carbonaceous materials (800–1900 cm^{-1}) is dominated by two bands at 1580 cm^{-1} (G-band) and 1350 cm^{-1} (D1-band).[46] The G-band corresponds to an ideal graphitic lattice vibration and involves the in-plane bond stretching motion of pairs of sp^2 hybridized carbon atoms.[47] If the size of the crystallites are small, a second band occurs around 1350 cm^{-1}, denoted as the D1-band, which reflects disorder in the system. This band is attributed to either defects or edges in the graphitic lattice, and is characteristic for the in-plane breathing vibrations of sp^2 bonded carbon within structural defects. A low intensity Raman band situated around 1610 cm^{-1} represents the edges of graphitic crystallites.[48] This shoulder of the G-band is referred to as the D2 band. A few bands of a low intensity complete the first-order Raman spectrum, *viz.*, bands around 1500 cm^{-1} (D3) and 1200 cm^{-1} (D4) pointing to amorphous carbon[49] and C–C and C=C vibrations,[50] respectively.

The second-order spectrum (2100–3500 cm^{-1}) consists of 4 bands;[51] the overtone of the D1 band (2 × D1) is the most important one since it is sensitive to the stacking of graphitic

layers.[52] The second-order spectrum is completed with a combination band at 2900 cm^{-1} (G + D1) and overtones at 3100 cm^{-1} (2 × D2) and 2400 cm^{-1} (2 × D4). To assess the contribution of the respective bands to the Raman spectra obtained, the spectra have been deconvoluted (see Experimental section).[35]

The Raman spectrum of the CCS after pyrolysis (Fig. 4) is representative for a highly disordered amorphous carbon. The G-band is positioned at 1592 cm^{-1}, a shift to higher wavenumbers compared to an ideal graphitic lattice. This shift is explained by the highly disordered nature of the amorphous carbon obtained (Fig. 2B and 3). The small graphitic domains have a high proportion of edges, as a result the D2-band becomes dominant.[53,54] The G- and D2-band are merged into a single band with a shift to the position of the D2 band. The broad D1 and 2 × D1 bands also point to a disordered carbon. Note that in all Raman spectra an additional band is found at *ca.* 1000 cm^{-1} which was found to be an artefact of the instrumental setup.

3.4. Interaction of the impregnated metal salts with CCS upon pyrolysis

Fig. 5A shows the XRD pattern of CCS loaded with $CuCl_2{\cdot}2H_2O$ after pyrolysis at T = 800 °C. The intensive and sharp maxima at 2θ = 50.9° and 59.5° show that the copper precursor has been completely reduced to fairly large fcc copper crystallites (loading of 3.2 wt% Cu, TGA (air), Fig. S5, ESI†). The broadening of the diffraction profile gives a weight-mean diameter of the copper crystallites of *ca.* 67 nm as calculated with the Scherrer equation (eqn (1)). According to XRD the amorphous carbon was not affected by the reduced copper particles.

Fig. 5B shows the XRD pattern of CCS loaded with $Ni(NO_3)_2{\cdot}6H_2O$ after pyrolysis at T = 800 °C. Reduction to fcc nickel crystallites is apparent from the reflections at 2θ = 52.3° and 61.1° (loading of 5.1 wt% Ni, Fig. S5, ESI†). The weight-mean diameter of the nickel crystallites is calculated to be *ca.* 59 nm. At an angle of 2θ = 30.2° a small peak is observed corresponding to the d(002) graphite reflection. Some reaction to graphitic carbon has occurred.

The XRD pattern of CCS loaded with $Co(NO_3)_2{\cdot}6H_2O$ after pyrolysis at T = 800 °C (Fig. 5C) shows broad maxima at 2θ = 52.0° and 60.8° indicating the transformation of the impregnated cobalt nitrate to fcc cobalt crystallites (loading of 1.5 wt% Co, Fig. S5, ESI†). The weight-mean diameter of the cobalt crystallites is *ca.* 36 nm. The maximum due to the d(002) reflection of graphite is considerably higher than the maximum displayed with nickel, which indicates that a more facile conversion to graphitic carbon has occurred.

Fig. 5D displays the XRD patterns measured on CCS loaded with $Fe(NO_3)_3{\cdot}9H_2O$ after pyrolysis at T = 800 °C. The maximum at 2θ = 52.5° indicates the presence of bcc iron crystallites (loading of 1.2 wt% of Fe, Fig. S5, ESI†). Maxima due to cementite, Fe_3C, are discernible at 2θ = 44.3°, 50.5°, 51.5°, 52.9°, 53.9°, and 57.9°. The weight-mean diameter of the iron crystallites is *ca.* 53 nm. It is important to note that the d(002) graphite reflection at 2θ = 30.2° has become dominant.

The extent of graphitisation of the CCS-support under the influence of the reduced metals (XRD) was further investigated

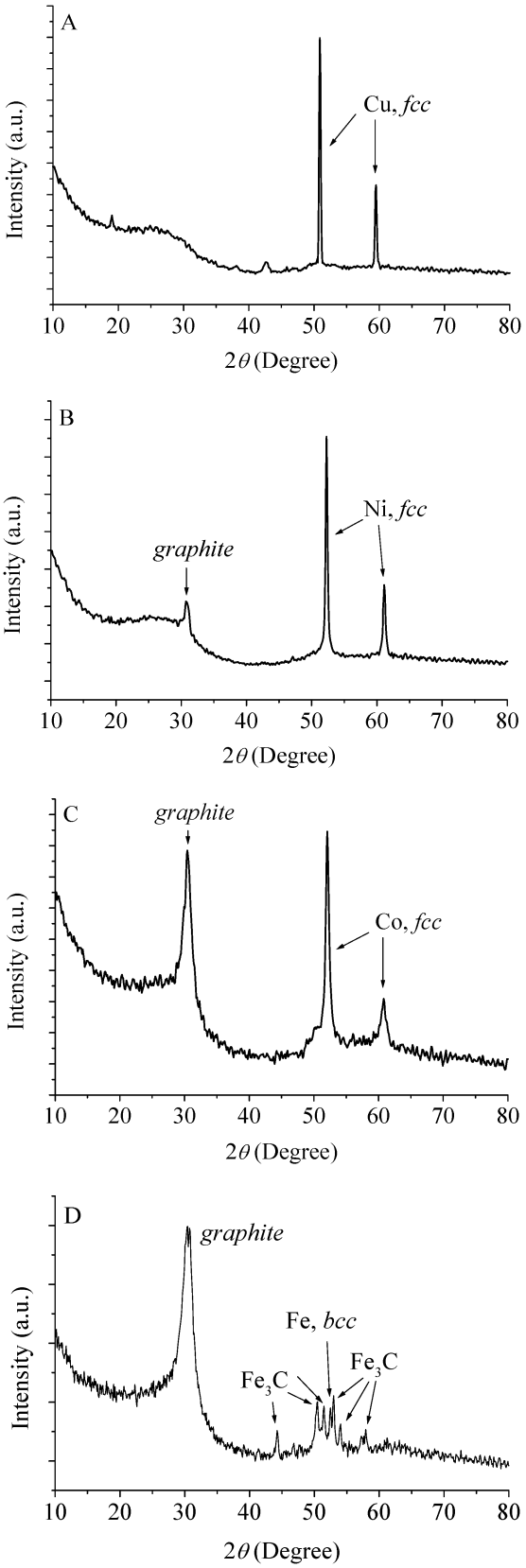

Fig. 5 XRD patterns of $CuCl_2{\cdot}2H_2O$ (A), $Ni(NO_3)_2{\cdot}6H_2O$ (B), $Co(NO_3)_2{\cdot}6H_2O$ (C) and $Fe(NO_3)_3{\cdot}9H_2O$ (D) loaded CCS after pyrolysis at T = 800 °C.

with Raman spectroscopy. The Raman spectrum of the copper loaded beads (Fig. S6a, ESI,† deconvolution results are reported in Table S2, ESI†) is nearly identical to that of the pristine beads (similar band positions and FWHM's), verifying that copper does not affect the amorphous carbon. Note that the sample showed some background fluorescence.

With nickel, being only moderately active in the graphitisation process according to XRD, the G + D2 band shifts to 1588 cm^{-1} (Fig. S6b and Table S2, ESI†). The 2 × D1 band narrows (FWHM = 172 cm^{-1} *vs.* 296 cm^{-1} for the CCS pyrolyzed in the absence of a metal salt). Both features indicate that some graphitisation of the amorphous carbon occurred.

Also for cobalt comparable observations were made, supporting the XRD data that graphitisation had occurred in the presence of cobalt. The G- and D2-band were clearly observed separately (Fig. S6c and Table S2, ESI†). The second-order spectrum could not be deconvoluted due to severe interference by background fluorescence.

Fig. 6A shows the Raman spectrum of CCS loaded with iron after pyrolysis at T = 800 °C, the most active graphitisation catalyst according to XRD. The spectrum shows an increased ordering of the carbon as compared to the amorphous carbon resulting from the pyrolysis of the unloaded CCS (compare with Fig. 4). The deconvolution results (Table S2, ESI†) show that the D1 band is clearly narrower (FWHM = 90 cm^{-1}), while the position of the G-band at 1580 cm^{-1} is in line with the presence of crystalline graphite.

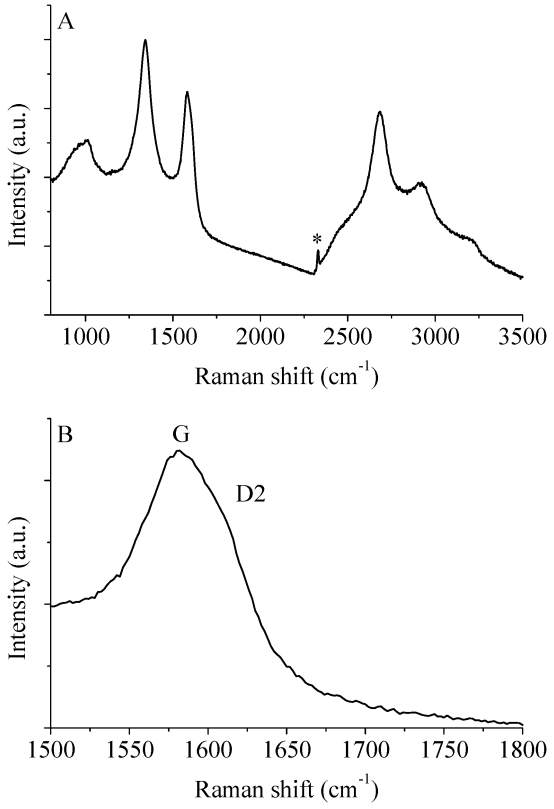

Fig. 6 Raman spectrum of the CCS loaded with $Fe(NO_3)_3 \cdot 9H_2O$ after pyrolysis at T = 800 °C (A, * = N_2) and magnification of the G-band (B). The D2-band (shoulder) is observed and is indicative for the edges of the graphitic material obtained.

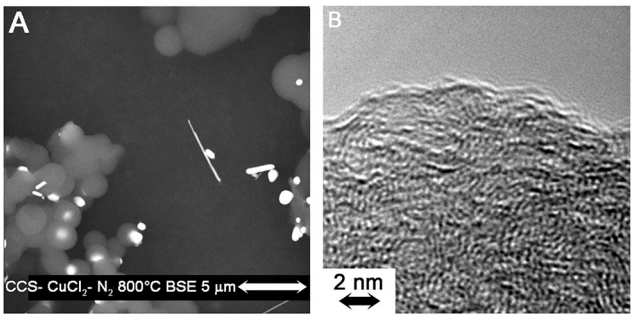

Fig. 7 SEM-BSE image of the external surface of CCS loaded with $CuCl_2 \cdot 2H_2O$ after pyrolysis at T = 800 °C (A), and HR-TEM image of the amorphous carbon obtained (B).

Fig. 6B shows the splitting of the G- and D2-band (1610 cm^{-1}), the D2-band pointing to the presence of edges of small graphitic crystallites. Also the 2 × D1 band at 2684 cm^{-1} (Fig. 6A) sharpens, the single band feature pointing to a turbostratic stacking of the graphitic layers.[55]

Fig. 7A represents a SEM-BSE image of CCS loaded with copper chloride after pyrolysis at T = 800 °C. A heterogeneous distribution of relatively large copper particles is observed. Besides the copper particles also some copper needles are observed. The copper chloride apparently crystallized as very thin platelets. Thermal decomposition and carbothermal reduction led to the copper needles. The size of the copper particles agrees with that obtained from XRD analysis. The HR-TEM image (Fig. 7B) shows the amorphous carbon obtained.

Fig. 8A represents a SEM-BSE image of a cluster of CCS impregnated with nickel nitrate and thermally treated at T = 800 °C. The small nickel particles on the carbon spheres are apparent as well as their heterogeneous dispersion. Fig. 8C represents a SEM image of an area more densely covered with nickel. Some graphitic carbon is observed which is not seen in the SEM-BSE image of Fig. 8D, which mainly displays the nickel particles. The TEM image (Fig. 8B) confirms the above results. The contrast of the nickel crystallites is due to Bragg reflection. Nickel crystallites represented at a lower contrast are not in a Bragg reflection position. Thin carbon layers around the nickel particles are observed as well as some graphitic nanoribbons. Nickel particles of a broad size range are displayed.

A heterogeneous distribution of cobalt particles results from the thermal treatment of CCS impregnated with cobalt nitrate (SEM, Fig. 9A). The encapsulation of the cobalt particles is evident from the SEM-BSE image (Fig. 9B). The formation of the graphitic layers underneath the cobalt particles is obvious from the fact that some cobalt particles appear to be only loosely connected to the carbon spheres. Fig. 9C shows a TEM image of a carbon sphere with encapsulated cobalt particles at the perimeter reflecting the core–shell morphology of the original CCS.

The catalytically active species ended up exclusively onto the shell leading to edge decoration of the spheres with metallic nanoparticles after pyrolysis. The nearly complete encapsulation

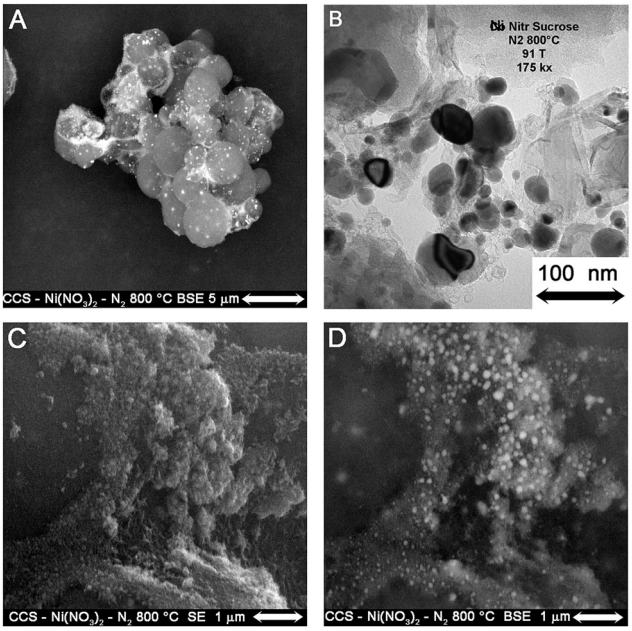

Fig. 8 SEM-BSE image of the external surface of CCS loaded with $Ni(NO_3)_2{\cdot}6H_2O$ after pyrolysis at T = 800 °C (A), TEM image (B), higher magnification. SEM (C) and SEM-BSE image (D).

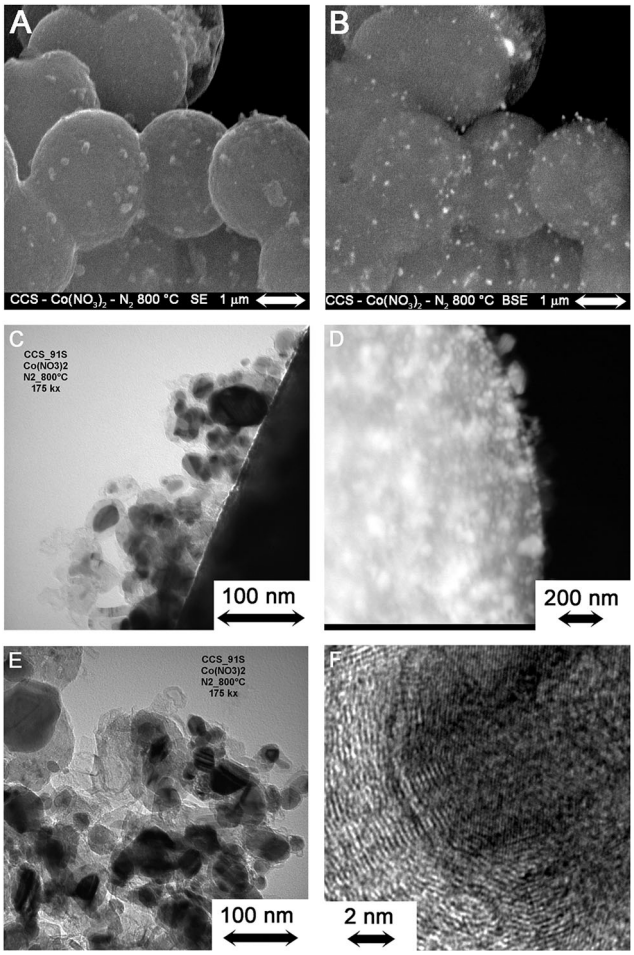

Fig. 9 EM images of CCS loaded with $Co(NO_3)_2{\cdot}6H_2O$ after pyrolysis at T = 800 °C, SEM and SEM-BSE images (A and B), TEM and STEM-HAADF images of the external surface (C and D), TEM image (E) and HR-TEM image (F) of a ground sample.

is evident as well as the fact that the cobalt particles appear to be separated slightly from the surface of the carbon sphere. The estimated thickness of the shell is, with *ca.* 100 nm, relatively thin. In the STEM-HAADF image (Fig. 9D) the location of the cobalt particles at the periphery of the CCS is confirmed. TEM shows graphite encapsulated cobalt particles of a diameter range of 5–70 nm as well as both graphitic and amorphous carbon (Fig. 9E). It is anticipated that the amorphous carbon exhibited in the centre of the figure originates from the original core. It is postulated that the hydrophobic core was not wetted during impregnation, therefore the core is unaffected and remains amorphous. The encapsulation is most obvious in the HR-TEM image of Fig. 9F.

Fig. 10A and B show a SEM and SEM-BSE image respectively of CCS impregnated with iron nitrate after pyrolysis at T = 800 °C. In the centre of the image some finely divided carbonaceous material is present with a high density of iron particles, which was released from the surface of the spheres due to extensive graphite formation. With TEM- and HR-TEM images (Fig. 10C and D) the extensive graphite formation is observed. The white arrow in Fig. 10C points to an iron nanoparticle responsible for the conversion of amorphous carbon to graphitic carbon.

The results point to the fact that during wet impregnation of the CCS the metal cations are adsorbed in the hydrophilic shell of the CCS. During pyrolysis at relatively low temperatures the metal salts are decomposed to the corresponding metal oxides which are subsequently reduced by the amorphous carbon of the decomposing CCS in a carbothermal reduction process at various temperatures. Both the temperature of reduction and the ability to form (metastable) metal carbides subsequently will govern the catalytic graphitisation process.

Ellingham diagrams (Fig. S2, ESI†) show that the copper oxide will reduce instantaneously to form copper nanoparticles. Copper, having near zero carbon solubility, does not react to a carbide.[56] Hence, conversion to metallic copper nanoparticles will occur but the amorphous carbon will not be converted into graphitic carbon.[57]

Nickel nitrate is converted to nickel oxide already below T = 300 °C. According to thermodynamics the carbothermal reduction to metallic nickel proceeded at about T = 440 °C. It is likely that the resulting metallic nickel particles form nickel carbide (Ni_3C) nanoparticles. When the (metastable) nickel carbide nanoparticles are heated above their decomposition temperature (T = 420 °C),[58] they become encapsulated within nanoshells of graphitic carbon.[59] The immobilised nickel particles therefore cannot cause a substantial recrystallization to graphitic carbon.

The reduction of cobalt starts at a higher temperature (T = 500 °C), it is anticipated that upon reduction metastable cobalt carbides (Co_2C, Co_3C) are formed. Their thermal decomposition temperature occurs around T = 485 °C,[60] hence, upon

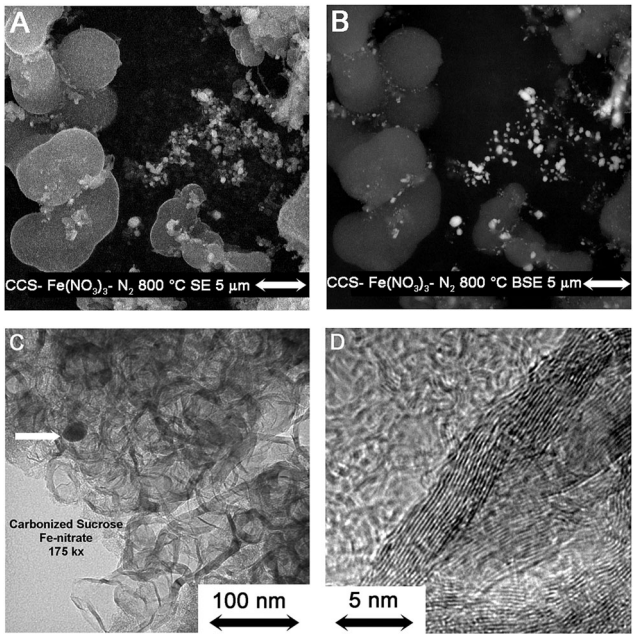

Fig. 10 SEM- and SEM-BSE image of the external surface of CCS loaded with $Fe(NO_3)_3{\cdot}9H_2O$ after pyrolysis at T = 800 °C (A and B), TEM- and HR-TEM image of the graphitic material obtained (C and D).

reduction of the cobalt, a fast formation and subsequent decomposition of cobalt carbide is anticipated, resulting in encapsulated cobalt particles. Since these processes occur at a higher temperature compared to nickel, a more pronounced graphitisation is observed.

The reduction of iron proceeds at a relatively elevated temperature (T = 700 °C), which brings about that the iron species become fairly mobile upon reduction, which explains the intensive graphitisation observed. The decomposition temperature of the iron carbides, such as cementite Fe_3C, is also around T = 700 °C,[60] which is in line with our experimental results.

While the positively charged metal cations will adhere to the surface *via* electrostatic interactions onto the partially negatively charged oxygen containing functional groups, the metal nanoparticles have to be supported differently on the CCS, since during pyrolysis the oxygen containing functionalities are removed from the surface. The interaction between metal nanoparticles and non-metallic surfaces is of a physical nature and is usually fairly weak.[61] The copper nanoparticles are likely held by the support by van der Waals interactions, similar to the interaction between copper nanoparticles and graphene.[62]

The situation with the nickel, cobalt and iron nanoparticles is different. They interact with the shell of the original CCS, thereby transforming it into graphitic species. This shell consisting of metal nanoparticles and graphitic nanoribbons is also likely held together to the core of the original CCS by van der Waals interactions. In Fig. 9C this is nicely demonstrated. Possibly there are some covalent bonds still present stemming for the original CCS that play a role in the interaction between the nanoparticles and graphitic material obtained on one side and the core on the other side.

4. Conclusions

Colloidal carbon spheres were obtained from the hydrothermal carbonisation of sucrose. *Via* ion exchange the colloidal carbon spheres were easily loaded with metal salts due to the presence of oxygen containing functional groups. Pyrolysis under inert conditions yielded supported metal nanoparticles. Firstly, a thermal decomposition of the metal salt yielded metal oxides. The carbon support subsequently reduced the metal oxides, which resulted in supported metal nanoparticles. The active species are exclusively positioned at the perimeter of the colloidal carbon spheres. This reflects the morphology of the colloidal carbon spheres, which consists of a hydrophobic core with a hydrophilic shell with oxygen containing functional groups. The method described here thus provides a means to obtain base metal nanoparticles deposited at the perimeter of a carbonaceous support.

Finally, the colloidal carbon support is affected by shell-decoration with metal nanoparticles. With the exception of copper nanoparticles, which cannot form copper carbides, the other metal nanoparticles are capable of (metastable) metal carbide formation and are active as catalysts in catalytic graphitisation. Whereas nickel shows only a moderate catalytic graphitisation activity, cobalt is more active and iron is most active.

Acknowledgements

We thanks AgentschapNL for financial support (*in situ* H_2O_2, project no. IS 043063).

Notes and references

1 A. Funke and F. Ziegler, *Biofpr*, 2010, **4**, 160.
2 Q. Wang, H. Li, L. Chen and X. Huang, *Carbon*, 2001, **39**, 2211.
3 X. Sun and Y. Li, *Angew. Chem., Int. Ed.*, 2004, **43**, 597.
4 M. Sevilla and A. B. Fuertes, *Chem. – Eur. J.*, 2009, **15**, 4195.
5 J. Ryu, Y. W. Suh, D. J. Suh and D. J. Ahn, *Carbon*, 2010, **48**, 1990.
6 M. M. Titirici, M. Antonietti and N. Baccile, *Green Chem.*, 2008, **10**, 1204.
7 N. Baccile, L. Guillaume, F. Babonneau, F. Fayon, M. M. Titirici and M. Antonietti, *J. Phys. Chem. C*, 2009, **113**, 9644.
8 D. Jagadeesan and M. Eswaramoorthy, *Chem. – Asian J.*, 2010, **5**, 232.
9 B. Hu, K. Wang, L. Wu, S. H. Yu, M. Antonietti and M. M. Titirici, *Adv. Mater.*, 2010, **22**, 813.
10 M. M. Titirici and M. Antonietti, *Chem. Soc. Rev.*, 2010, **39**, 103.
11 M. M. Titirici, A. Thomas and M. Antonietti, *New J. Chem.*, 2007, **31**, 787.
12 M. Sevilla, J. A. Maciá-Agulló and A. B. Fuertes, *Biomass Bioenergy*, 2011, **35**, 3152.
13 J. P. Paraknowitsch, A. Thomas and M. Antonietti, *Chem. Mater.*, 2009, **21**, 1170.
14 H. Choi, S.-J. Ko, Y. Choi, P. Joo, T. Kim, B. R. Lee, J.-W. Jung, H. J. Choi, M. Cha, J.-R. Jeong, I.-W. Hwang, M. H. Song,

B.-S. Kim and J. Y. Kim, *Nat. Photonics*, 2013, **7**, 732, and references cited therein.
15 P. Makowski, R. Demir Cakan, M. Antonietti, F. Goettman and M. M. Titirici, *Chem. Commun.*, 2008, 999.
16 H. S. Qian, M. Antonietti and S. H. Yu, *Adv. Funct. Mater.*, 2007, **17**, 637.
17 L. S. Zhang, W. Li, Z. M. Cui and W. G. Song, *J. Phys. Chem. C*, 2009, **113**, 20594.
18 G. Yu, B. Sun, S. Xie, S. Yan, M. Qiao, K. Fan, X. Zhang and B. Zong, *J. Am. Chem. Soc.*, 2010, **132**, 935.
19 H. Sun, G. Zhou, S. Liu, H. M. Ang, M. O. Tadé and S. Wang, *ACS Appl. Mater. Interfaces*, 2012, **4**, 6235.
20 W. Teunissen, A. A. Bol and J. W. Geus, *Catal. Today*, 1999, **48**, 329.
21 W. Zhang, *J. Nanopart. Res.*, 2003, **5**, 323.
22 Y. Yin, Z.-Y. Li, Z. Zhong, B. Gates, Y. Xia and S. Venkateswaran, *J. Mater. Chem.*, 2002, **12**, 522.
23 K. R. Reddy, B. C. Sin, C. H. Yoo, W. Park, K. S. Ryu, J.-S. Lee, D. Sohn and Y. Lee, *Scr. Mater.*, 2008, **58**, 1010.
24 J. Zielinski, I. Zglinicka, L. Znak and Z. Kaszkur, *Appl. Catal., A*, 2010, **381**, 191.
25 C. I. Meyer, S. I. Regenhardt, A. J. Marchi and T. F. Garetto, *Appl. Catal., A*, 2012, **417–418**, 59.
26 V. Schröder, B. Emonts, H. Janßen and H.-P. Schulze, *Chem. Eng. Technol.*, 2004, **27**, 847.
27 J. Hoekstra, M. Versluijs-Helder, E. J. Vlietstra, J. W. Geus and L. W. Jenneskens, *ChemSusChem*, 2015, **8**, 985.
28 B. K. Pradhan and N. K. Sandle, *Carbon*, 1999, **37**, 1323.
29 C. Moreno-Castilla, M. V. López-Ramón and F. Carrasco-Marín, *Carbon*, 2000, **38**, 1995.
30 M. L. Toebes, J. M. P. van Heeswijk, J. H. Bitter, J. van Dillen and K. P. de Jong, *Carbon*, 2004, **42**, 307.
31 T. G. Ros, J. van Dillen, J. W. Geus and D. C. Koningsberger, *Chem. – Eur. J.*, 2002, **8**, 1151.
32 Z. Wu, C. U. Pittman and S. D. Gardner, *Carbon*, 1995, **33**, 597.
33 A. A. Pirzado, L. Truong-Phuoc, V. Papaefthimiou, C. Matei Ghimbeu, F. Le Normand, H. Ba, T. Thanh-Tung, C. Pham-Huu and I. Janowska, *J. Colloid Interface Sci.*, 2015, **451**, 221.
34 A. L Patterson, *Phys. Rev.*, 1939, **56**, 978.
35 A. Sadezky, H. Muckenhuber, H. Grothe, R. Niessner and U. Pöschl, *Carbon*, 2005, **43**, 1731.
36 B. V. L'vov and A. V. Novichikhin, *Spectrochim. Acta, Part B*, 1995, **50**, 1459.
37 W. Brockner, C. Ehrhardt and M. Gjikai, *Thermochim. Acta*, 2007, **456**, 64.
38 C. Ehrhardt, M. Gjikai and W. Brockner, *Thermochim. Acta*, 2005, **432**, 36.
39 K. Wieczorek-Ciurow and A. Kozak, *J. Therm. Anal. Calorim.*, 1999, **58**, 647.
40 P. L. Walker Jr., F. Rusinko Jr. and L. G. Austin, in *Advances in Catalysis*, ed. D. D. Eley, P. W. Selwood and P. B. Weiss, Academic Press, New York, 1959, vol. 11, p. 133.
41 J. Hunt, A. Ferrari, A. Lita, M. Crosswhite, B. Ashley and A. E. Stiegman, *J. Phys. Chem. C*, 2013, **117**, 26871.
42 L. Yu, C. Falco, J. Weber, R. J. White, J. Y. Howe and M. M. Titirici, *Langmuir*, 2012, **28**, 12373.
43 S. Kubo, I. Tan, R. J. White, M. Antonietti and M. M. Titirici, *Chem. Mater.*, 2010, **22**, 6590.
44 H. Fujimoto, *Carbon*, 2003, **41**, 1585.
45 Z. Q. Li, C. J. Lu, Z. P. Xia, Y. Zhou and Z. Luo, *Carbon*, 2007, **45**, 1686.
46 F. Tuinstra and J. L Koenig, *J. Chem. Phys.*, 1970, **53**, 1126.
47 A. C. Ferrari and J. Robertson, *Phys. Rev. B: Condens. Matter Mater. Phys.*, 2000, **61**, 14095.
48 L. M. Malard, M. A. Pimenta, G. Dresselhaus and M. S. Dresselhaus, *Phys. Rep.*, 2009, **473**, 51.
49 T. Jahwari, A. Roid and J. Casado, *Carbon*, 1995, **33**, 1561.
50 B. Dipper, H. Jander and J. Heintzenberg, *Phys. Chem. Chem. Phys.*, 1999, **1**, 4707.
51 A. Cuesta, P. Dhamelincourt, J. Laureyns, A. Martinez-Alonso and J. M. D. Tascon, *Carbon*, 1994, **32**, 1523.
52 L. G. Cançado, A. Reina, J. Kong and M. S. Dresselhaus, *Phys. Rev. B: Condens. Matter Mater. Phys.*, 2008, **77**, 245408.
53 R. Escribano, J. J. Sloan, N. Siddique, N. Sze and T. Dudev, *Vib. Spectrosc.*, 2001, **26**, 179.
54 S. K. Sze, N. Siddique, J. J. Sloan and R. Escribano, *Atmos. Environ.*, 2001, **35**, 561.
55 M. A. Pimenta, G. Dresselhaus, M. S. Dresselhaus, L. G. Cançado, A. Jorio and R. Saito, *Phys. Chem. Chem. Phys.*, 2007, **9**, 1276.
56 C. P. Deck and K. Vecchio, *Carbon*, 2006, **44**, 267.
57 J. Hoekstra, A. M. Beale, F. Soulimani, M. Versluijs-Helder, J. W. Geus and L. W. Jenneskens, *J. Phys. Chem. C*, 2015, **119**, 10653.
58 Y. Leng, F. Xie, F. Liao and X. Li, *Thermochim. Acta*, 2008, **473**, 43.
59 Z. L. Schaefer, M. L. Gross, M. A. Hickner and R. E. Schaak, *Angew. Chem., Int. Ed.*, 2010, **49**, 7045.
60 L. Ni, K. Kuroda, L.-P. Zhou, K. Ohta, K. Matsuishi and J. Nakamura, *Carbon*, 2009, **47**, 3054.
61 P. Benjamin and C. Weaver, *Proc. R. Soc. London*, 1959, **A252**, 418.
62 P. Lazar, S. Zhang, K. Safarova, Q. Li, J. P. Froning, J. Granatier, P. Hobza, R. Zboril, F. Besenbacher, M. Dong and M. Otyepka, *ACS Nano*, 2013, **7**, 1646.
63 M. Hesse, H. Meier and B. Zeeh, *Spektroskopische Methoden in der Organischen Chemie*, Thieme, Stuttgart, 8th edn, 2011.